Journal of the European Ceramic Society 20 (2000) 2009–2024

Mechanical stability of $BaTiO_3$-based PTC thermistor components: experimental investigation and theoretical modelling

Peter Supancic *

Institute of Structural and Functional Ceramics, University of Leoben, Materials Center, Peter-Tunner Straβe 5, A-8700 Leoben, Austria

Received 16 December 1999; accepted 19 March 2000

Abstract

Barium titanate based positive temperature coefficient (PTC) thermistors, especially high power switching devices, can suffer major mechanical damage if inhomogeneous heating occurs under an applied electrical voltage. The main mode of mechanical failure, known as delamination fracture, manifests itself by cracking of the ceramic disc along a plane approximately parallel to the electrodes. This damage results from the build-up of thermal stresses, the amplitude of which is governed by a large number of geometrical, electrical and thermo-elastic parameters. For an experimental investigation, a measurement device was set up to observe the electrical behaviour of PTC-components during the switching process. To interpret specific aspects of the observations, a mathematical model was developed to simulate the electrical, thermal and thermo-elastic behaviour. In addition to the resistance/temperature characteristics considered by other authors, the varistor-effect (i.e. the non-linear isothermal current-voltage behaviour which is thought to make a significant contribution to the development of the mechanical stresses inparticular) is also taken into account. By doing a non-linear analysis with one and two dimensional models, and taking all relevant temperature dependencies of the material properties into account, a qualitative and quantitative agreement with the experimentally determined electro-thermal and failure statistical behaviour could be achieved. It is shown that in addition to the resistance/temperature characteristics, it is very important to account for the varistor-effect when modelling the build-up of the mechanical stresses during the switching process.

Keywords: $BaTiO_3$ and titanates; Electrical properties; Failure analysis; PTC devices

1. Introduction

Positive temperature coefficient (PTC) thermistors are characterised by an increase in the electrical resistance with temperature. Apart from special polymer composites (so-called Polyswitch-PTCs), commercial PTC-components are based on a doped, polycrystalline, *n*-semiconducting barium-titanate ($BaTiO_3$) ceramic. A ferroelectric–paraelectric phase transition at a critical temperature (the Curie-temperature) in combination with screening effects of potential barriers at grain boundaries causes the exceptionally strong PTC-effect — encompassing a resistance increase of several orders of magnitude within a temperature interval of a few tens of degrees.[1–5] On the one hand, PTC components are used for passive applications as temperature and level sensors. On the other hand, PTC-resistors can be used as active (heat-generating) components, e.g. as self-regulating switching devices for degaussing, heating and overload-protection applications. However, when used as power devices mechanical failure can occur during high-power switching processes, which limits the magnitude of the applied electrical voltage.

Several types of mechanical failures of PTC-components have been reported in literature.[6–8] Apart from irregular cracking and chipping of ceramic edges, delamination fracture can split the whole component (which is usually formed as a cylindrical disc with metallic electrodes covering the two base surfaces) into two parts. A typical example of a delaminated component is shown in Fig. 1.

In principle, all of these mechanical failure modes are caused by thermal stresses induced by an inhomogeneous temperature field within the self-heated ceramic component. By doing infrared microscopy Mader et al.[9] found temperature differences up to 50°C within single large grains. While irregular cracking and edge chipping

* Tel.: +43-3842-4029109; fax: +43-3842-4029102.
E-mail address: phs@unileoben.ac.at

0955-2219/00/$ - see front matter
PII: S0955-2219(00)00100-X

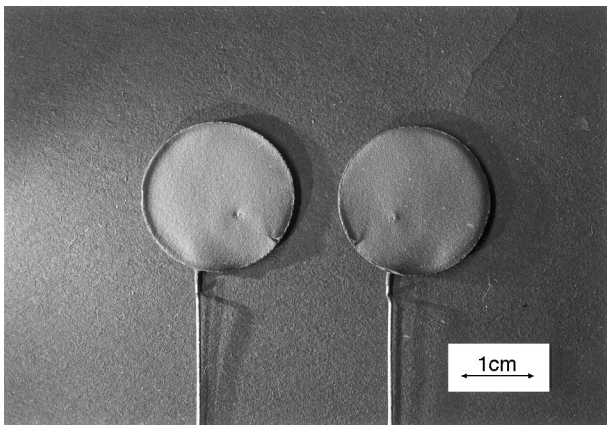

Fig. 1. Delaminated PTC-component (split into two parts).

indicate a non-optimised electrode design[10] and/or heterogeneities in the ceramic disc, delamination fracture is a consequence of intrinsically induced thermal stresses even in an homogenous and well-designed component. The occurrence of the underlying thermal gradients are understood qualitatively and have been studied in computer simulations. While some authors have considered only the thermo-electrical behaviour during the switching process under varying boundary conditions[12], Dewitte et al.[11] have additionally performed a thermo-elastic analysis. Basically, it was found that surface heat-losses through the electrodes, where contacting wires are mounted, lead to a hotter centre during the highly transient switching process. The amplitudes of the corresponding thermal stresses are highly dependent on the applied boundary conditions, i.e. the kind of environment or the presence of solder to fix the contacting wire. In general, however, the calculated mechanical stresses in a homogeneous PTC-component are too low to explain delamination fracture. As one possible explanation, it has been postulated that higher stress-amplitudes may be a consequence of inhomogeneities in the resistance field within the ceramic body.

In this paper, models presented previously in literature to explain delamination fracture in homogeneous samples, are modified by accounting for the varistor-effect within the resistance-temperature characteristics. The results of this adapted and comprehensive model of the electrical, thermal and elastic behaviour of a PTC-component in a typical switching application are compared with experimental observations. In addition a fracture statistical analysis is performed to interpret the observed cracking and failure mechanisms. The exceptionally good agreement between modelling and empirical results indicates, that the varistor-effect significantly changes the thermo-electrical response of the component, and in consequence also the build-up of thermo-mechanical stresses. Therefore, the varistor-effect must play an integral role in modelling of such components.

2. Experimental procedure

2.1. Description and properties of specimens

Special trial (commercial-type) PTC-components were supplied by Siemens/Matsushita (Deutschlandsberg, Austria). The geometry of the component is shown in Fig. 2. The $BaTiO_3$-based ceramic body is disc-shaped with a diameter of 3 mm and a thickness of 2.5 mm. Both flat surface areas of the disc are coated with a chromium–nickel–silver electrode, which is sputtered on to a thickness of about 0.3 μm. The uncovered gap between the circular electrode layer and the rim of the disc is less than 0.1 mm. A tin-coated copper wire is attached to the electrodes by solder, which consists of a lead-tin-silver alloy (melting point: 300°C).

To characterise the PTC-component with respect to the switching behaviour, the relevant material properties were measured to provide data for the simulation. Since the macroscopic, continuum-mechanical approach to PTC-components under the assumption of isotropy is taken in this paper, only the corresponding macroscopic scalar properties are required. These are: the resistance/temperature characteristics including the varistor-effect, the heat capacity, the thermal conductivity, the thermal expansion coefficient, two independent elastic moduli, and the mass density. Since there is a natural variation of these properties for individual components within one batch, a testing set, defined by a specific resistance at 25°C in the range of 36±1 Ω cm, was selected. The required properties were measured for a few samples and suitable mean values were determined. In the following sections, these properties and their temperature-dependences are described.

2.1.1. Resistance/temperature characteristics including the varistor-effect

The fundamental electrical property of the PTC-material is the dependence of the electrical resistance

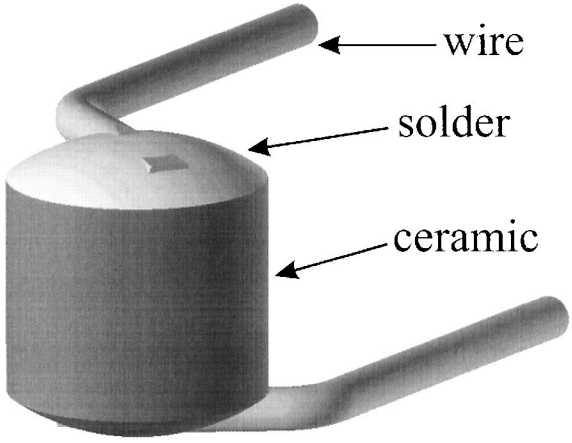

Fig. 2. Geometry of PTC-sample.

$\rho(T, E)$ on temperature T and electrical field strength E. In Fig. 3, the solid line shows the relation between the normalised resistance and temperature, measured in the temperature range from 20 to 300°C under nominally zero electrical load (i.e. about 1 V/cm). The key features of this measured curve are summarised in Table 1.

While a slight decrease of the resistance with respect to the temperature (negative temperature coefficient, NTC) is found at room temperature, the actual PTC range (which is marked in Fig. 3 from T_{min} to T_{max}) spans a temperature interval from 60 to 230°C. The temperature of the onset of the steep resistance rise, which is called the reference temperature T_{ref}, is found at 120°C. After passing a resistance maximum at T_{max}, a further NTC range is found. Additionally to the temperature dependence a strong variation of the resistance with respect to the electrical field strength is found in these materials.[13] At any given temperature the resistance drops with increasing electrical field strength. Referring to "varistors" (voltage dependent resistors), this resistance lowering effect is called varistor-effect. In Fig. 3, measured resistance/temperature characteristics at higher field strengths up to 1.5 kV/cm are plotted as symbols. To provide a continuous function for the simulations, datapoints were fitted (see dashed and dotted curves in Fig. 3) by a procedure described in Appendix A. The strongest varistor-effect, i.e. a resistance drop of more than one order of magnitude between zero-load and a field strength of about 1.5 kV/cm, is found around the temperature $T_{\alpha_{max}}$ at about 145°C, where the maximum of resistance-increase α_{max} occurs.

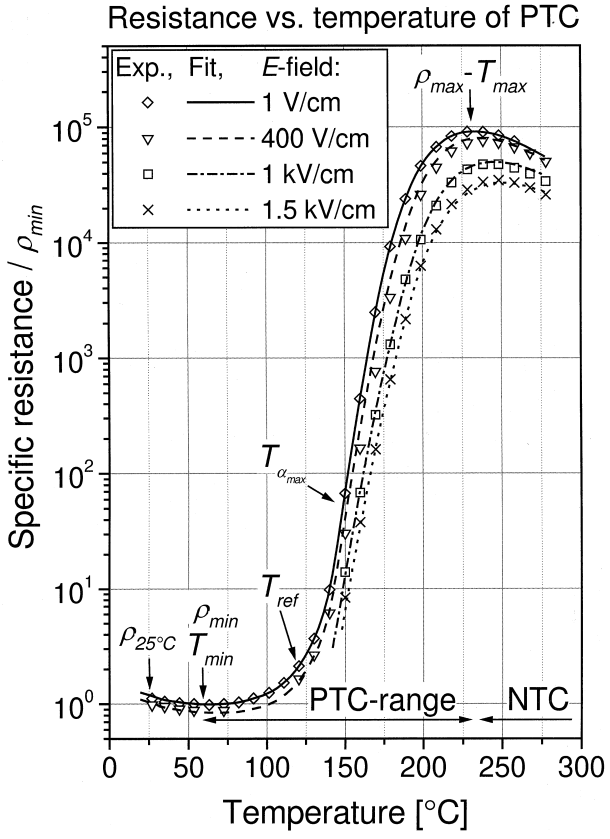

Fig. 3. Resistance/temperature characteristics (normalised to ρ_{min}) at various electrical field strengths, measured by Siemens/Matsushita.[14]

This observed electrical behaviour can be explained qualitatively by the following consideration. The total resistance of PTC-ceramics is compounded from a network of grain and grain-boundary transition resistances. Grain-boundaries in particular are decisive for the PTC thermistor resistance, because they build-up strong potential barriers at temperatures above T_{ref}. These barriers and the corresponding transition resistances are primarily influenced by high electric field strengths. While at low temperatures the total resistance lowering effect of high fields is small, since a significant portion of the applied voltage is attributable to the grain resistance, in the high temperature state the varistor-effect is much stronger, because the resistance is dominated by the grain-boundary barriers.

2.1.2. Heat capacity

The heat capacity as a function of temperature of this PTC-material was measured by I. Hahn (Siemens, Munich).[15] The experimental data were fitted using function (2.1) as presented by Dewitte et al.:[11]

$$c_p(T) = c_{c,0} \cdot \left[1 + c_{c,1} \cdot \theta + c_{c,2} \cdot \exp\left[\pm c_{c,3} \cdot \theta\right]\right], \qquad (2.1)$$

whereby θ the non-dimensional temperature defined as $\theta = \frac{T - T_C^{cp}}{T_C^{cp}}$ (where T_C^{cp} is the nominal phase transition temperature), was used to determine the specific coefficients of this material as $c_{c,0} = 481$ J/kg°C, $c_{c,1} = 0.021$, $c_{c,2} = 0.158$ and $c_{c,3} = 8.3$.

Table 1
Key features of the measured resistance/temperature characteristics curve at zero load

Symbol	Value	Temperature	Description
$\rho_{25°C}$	36 Ω cm	25°C	Specific resistance at 25°C room temperature
ρ_{min}	30 Ω cm	60°C	Minimum of specific resistance at T_{min}
ρ_{ref}	60 Ω cm	120°C	Specific reference resistance at T_{ref}, defined by: $\rho_{ref} = 2 \cdot \rho_{min}$, (onset of steep resistance rise)
α_{max}	20% /°C	145°C	Maximum of slope in the PTC-range at $T_{\alpha_{max}}$: $\alpha_{max} = \mathrm{Max}\left(\frac{1}{\rho} \cdot \frac{\partial \rho}{\partial T}\right)$
ρ_{max}	300 kΩ cm	230°C	Maximum of specific resistance at T_{max}

In Fig. 4 the measured data and the corresponding fitted curve are shown as symbols and a solid line respectively. $T_C^{c_p}$ can be determined from the peak in this curve as 146°C.

2.1.3. Thermal conductivity

The measured thermal conductivity was found to be between 2 and 3 W/mK in the temperature range of interest. To facilitate comparison with the work of Dewitte et al.[11] and remaining within the range of measurements on this material,[15] the temperature-independent value of the thermal conductivity λ was assumed to be 2.5 W/mK.

2.1.4. Heat expansion coefficient

Dilatometry on small beam samples in air (NETSCH Dilatometer) was used to determine the linear thermal expansion coefficient α of the PTC-material. A plot of the measured data, presented as symbols in Fig. 5, shows two different levels below and above the nominal phase transition temperature T_C^{α} (in this case at about 140°C, corresponding to the peak in this curve). During the phase transition a volume contraction occurs and the differential thermal expansion coefficient becomes negative. In a procedure analogous to that applied by Dewitte et al.,[11] the following function was chosen to fit the observed temperature-dependence:

$$\alpha(T) = \begin{cases} c_{\alpha,1} - \dfrac{c_{\alpha,2}}{1 + c_{\alpha,3}\cdot\left(T - T_C^{\alpha}\right)^2}, & \text{for} \quad T < T_C^{\alpha} \\ c_{\alpha,4} - \dfrac{c_{\alpha,4} - c_{\alpha,1} + c_{\alpha,2}}{1 + c_{\alpha,5}\cdot\left(T - T_C^{\alpha}\right)^2}, & \text{for} \quad T \geqslant T_C^{\alpha} \end{cases} \tag{2.2}$$

where $c_{\alpha,i}$ ($i = 1,..5$) represent the coefficients of fitting. While the plateau values $c_{\alpha,1}$ and $c_{\alpha,4}$ differ by a factor of nearly 3, the asymmetric Lorentz-function based part-functions in relationship (2.2), centred at T_C^{α}, takes the volume contraction into account. The values of the coefficients in relationship (2.2), which were calculated by a non-linear fit-routine, and their interpretation are summarised in Table 2. The corresponding plot of this function is given in Fig. 5 as a solid line.

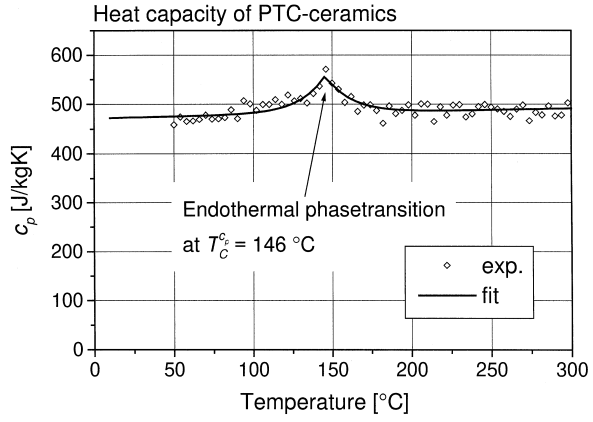

Fig. 4. Heat capacity as a function of temperature; measured by I. Hahn (Siemens Munich).[15]

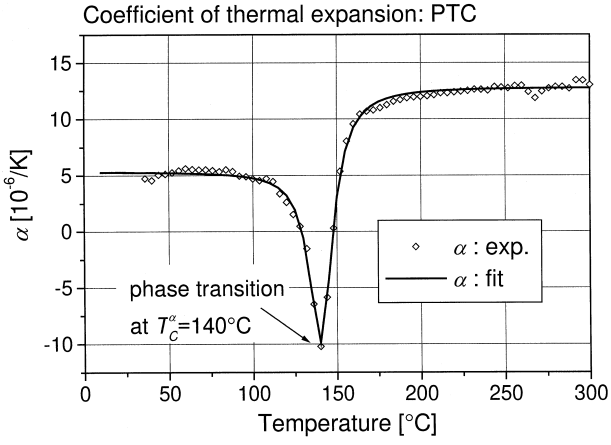

Fig. 5. Linear, differential thermal expansion coefficient as a function of temperature; measured data and fitted curve.

2.1.5. Elastic moduli

Under the assumption of an isotropic elastic behaviour, two elastic moduli, namely the Young's modulus and the Poisson's ratio are required to describe the elastic behaviour. These quantities were measured by I. Hahn[15,16] (Siemens, Munich) as a function of temperature. While the Poisson's ratio has a value of about 0.3 over the temperature range of interest, the observed temperature dependence of the Young's modulus, as determined by two independent experimental methods (namely a static bending and a resonance method), are dramatic. In Fig. 6 the measured data values are plotted with respect to temperature. A regression function of the form

$$Y(T) = \begin{cases} c_{Y,1} + c_{Y,2}\cdot T, & \text{for} \quad T < T_C^{Y} \\ c_{Y,3} - (c_{Y,3} - c_{Y,1} - c_{Y,2}\cdot T_C^{Y}) & \\ \exp\left[-c_{Y,4}(T - T_C^{Y})\right], & \text{for} \quad T \geqslant T_C^{Y} \end{cases} \tag{2.3}$$

was chosen to fit the measured data. In the temperature range below the nominal phase transition temperature T_C^{Y}, a straight line is used to fit the slightly falling trend. Passing the phase transition temperature a sudden

Table 2
Values of parameters for Eq. (2.2)

Parameter	Value	Interpretation
T_C^{α}	140 °C	Nominal Curie-temperature according to α
$c_{\alpha,1}$	$5.22\cdot10^{-6}$ °C^{-1}	Plateau level below T_C^{α}
$c_{\alpha,2}$	$10.0\cdot10^{-6}$ °C^{-1}	Height of peak at T_C^{α}
$c_{\alpha,3}$	0.0158 °C^{-2}	Measure of peak width below T_C^{α}
$c_{\alpha,4}$	$12.8\cdot10^{-6}$ °C^{-1}	Plateau level above T_C^{α}
$c_{\alpha,5}$	0.00769 °C^{-2}	Measure of peak width above T_C^{α}

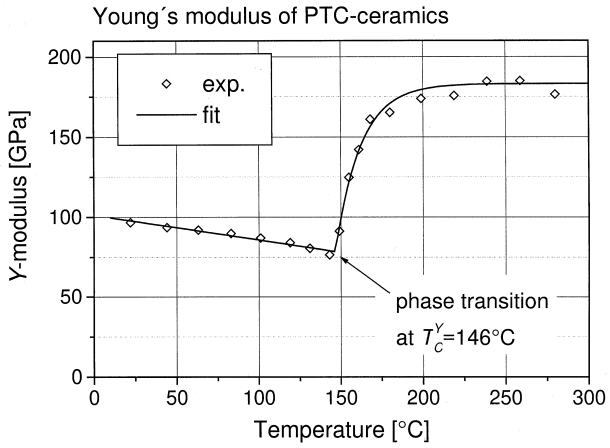

Fig. 6. Young's modulus, as a function of temperature; measured data and fitted curve.[15,16]

increase occurs and finally a plateau-value of about twice the magnitude of Y in the ferroelectric state is reached. Mathematically an exponential function shows the expected property. The parameters $c_{Y,1}$ ($i=1,..4$) in relationship (2.3) are calculated by a non-linear fit-routine and are summarised in Table 3. In literature a similiar, but less dramatic temperature-dependence of the Young's modulus is reported.[17]

2.1.6. Mass density

The mass density ρ_m was determined by the Archimedian method to the value of 5.66 g/cm^3 and is considered as independent from temperature.

It should be noted that, for the PTC-ceramics of this study, the structural phase transition, as indicated by peaks in the temperature-dependent behaviour of the heat capacity ($T_C^{c_p}$), the thermal expansion (T_C^{α}) and the Young's modulus (T_C^Y), occurs in the temperature range between 140 and 146°C. It is within this range that the strongest increase α_{max} of the PTC resistance/temperature characteristics is found. This is above the reference temperature T_{ref}, which is often misleadingly taken to be equivalent to the phase transition temperature.

2.2. Experimental set-up

To observe the electrical behaviour of the PTC-component during the switching process under different applied voltages, a measurement device was set-up as shown schematically in Fig. 7. The primary circuit consist of a serial connection of the considered PTC-component and a shunt resistor with a fixed resistance R_V, which is driven by an AC (50 Hz) or DC voltage source. The total voltage W and the potential drop at the shunt resistor V are monitored over time with a sampling rate of 50 kHz. While the voltage drop V within the shunt resistor is proportional to the integral current J according to the Ohmic law

$$J = \frac{V}{R_V}, \tag{2.4}$$

the actual total resistance of the PTC-component R_{PTC} can be expressed by

$$R_{PTC} = R_V \cdot \frac{W - V}{V} = R_V \cdot \frac{U}{V}, \tag{2.5}$$

where U is the total (integral) voltage drop within the PTC-component. The PTC samples were tested by an single switch cycle, where the voltage was applied to the circuit for several seconds, so that the high temperature state of the PTC ceramics is reached. Then the relay was opened again. After a sufficient cooling time, the resistance of the sample at room temperature $\rho_{25°C}$ was measured again and compared with the value before the electrical test. If the change in resistance is larger than 3%, it is assumed that mechanical damage of the PTC-resistor occurred, the transient signal of which can be found as a discontinuity in the monitored voltage data (compare to[6]). Smaller resistance shifts are not significant and the corresponding samples are meant to be regular and undamaged. Different voltages were applied to find the limits of strength of the actual batch of PTC-components,

Table 3
Values for parameters used in relationship (2.3)

Parameter	Value	Interpretation
T_C^Y	146°C	Nominal Curie-temperature according to Y
$c_{Y,1}$	101×10^9 Pa	Plateau level below T_C^Y
$c_{Y,2}$	156×10^9 Pa/°C	Slope of Y in the low-temperature range
$c_{Y,3}$	183×10^9 Pa/°C	Plateau level above T_C^Y
$c_{Y,4}$	0.0637 °C^{-1}	Measure of the width of the step at T_C^Y

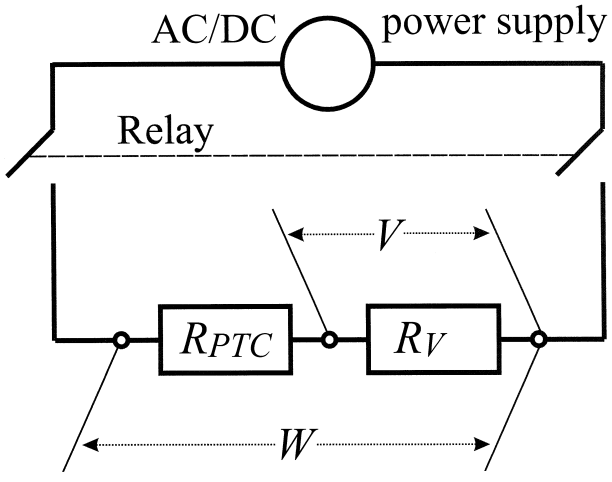

Fig. 7. Experimental set-up to measure applied voltage W and current according Eq. (2.4).

whilst maintaining the resistance of the shunt resistor at 1 kΩ. According a typical operational profile the resistance of the shunt should be 7–8 times larger than the total resistance of the PTC-components at room temperature. The results of this testing procedure will be discussed together with the results of the simulation in Section 4.

3. Theoretical modelling

The general theoretical approach is similar to that adopted by Dewitte et al.[11] The primary aim is to calculate the thermo-mechanical loading, caused by current-driven heat production during the PTC switching process. In general, a coupled electrical-thermal-mechanical problem has to be solved. The physical interactions in such a coupled PTC-system are shown schematically in Fig. 8. If some reasonable simplifications are made and appropriate approximations applied, a set of relatively clear equations can be obtained. By assuming quasi-static, uncoupled thermoelasticity, it is possible to separate the thermal and the mechanical components of the problem. This is a reasonable assumption to make considering the PTC-switching process, because (i) the rate of thermal straining during the thermal expansion is relatively slow in terms of the velocity of sound in the material, so that inertia effects can by neglected, and (ii) omitting the thermo-mechanical coupling term leads, in this case, only to a small error, since on the one hand the energy expended in the PTC-component is dominated by the Joule heating and on the other hand, temperature changes due to thermo-mechanical couplings are generally small in non-plastic materials such as ceramics. While the mechanical equations of thermoelasticity[18] can be solved separately by using standard methods (in this case the FEM program ANSYS® was used), the electro-thermal equations have to be considered together, since the PTC-resistance/temperature-characteristics inherently couple the electrical current and the temperature.

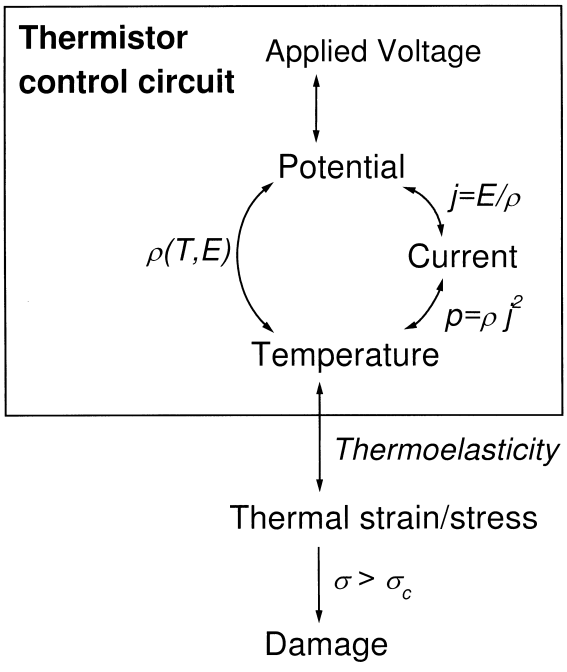

Fig. 8. Coupled physical processes involved in a PlC-switching process.

The thermal part of this set of coupled differential equations to describe the electro-thermal processes of the thermistor-component is given by the well-known heat transfer equation[19,20]

$$c_p(T)\cdot\rho_m\frac{\partial T(t,\vec{x})}{\partial t}=\vec{\nabla}\left[\lambda\cdot\vec{\nabla}T(t,\vec{x})\right]+p(t,\vec{x}) \quad (3.1)$$

which describes the temperature field $T(t,\vec{x})$ in respect to time- and space. The previously discussed material properties have to taken into account, namely the heat capacity c_p, the mass density ρ_m and the heat conductivity λ. The source term $p(t,\vec{x})$ is given by the Joule heating rate per unit volume according to the electrical power

$$p(t,\vec{x})=\rho(T(t,\vec{x}),E(t,\vec{x}))\cdot j^2(t,\vec{x}), \quad (3.2)$$

where j is the absolute value of the local electric current density $\vec{j}$, which is proportional to the electric field strength and the local conductivity σ (reciprocal to ρ):

$$\vec{j}=\sigma(T,E)\cdot\vec{E}=\frac{1}{\rho(T,E)}\cdot\vec{E}. \quad (3.3)$$

Neglecting internal currents due to the existence of polarisation charge, which may play an important role at frequencies of the applied AC voltage source above several hundred Hertz due to effects of the capacity (for applications in the "high frequency" range, the complex resistance/temperature characteristics, according to the Ohmic and capacitive contributions, has to be taken into account), leads to a vanishing divergence of the current density

$$\vec{\nabla}\cdot\vec{j}=0 \quad (3.4)$$

Introducing the electric potential ϕ by

$$\vec{\nabla}\phi=-\vec{E} \quad (3.5)$$

leads to the expression

$$\Delta\phi=\frac{1}{\rho(T,E)}\vec{\nabla}\rho(T,E)\cdot\vec{\nabla}\phi, \quad (3.6)$$

which is a highly non-linear partial differential equation and generally can be solved only iteratively. Neglecting

the $\vec{E}$-field-dependence of the resistance leads to the well-published[11,12] linearized form of Eq. (3.6).

In this work, a one dimensional approach is considered to tackle the electro-thermal part of the model (this notwithstanding a three-dimensional model is applied to the thermo-elastic analysis). Consequently, the partial differential Eq. (3.6) becomes an ordinary non-linear differential equation, which is solved by a computer code based on the finite difference method. For the chosen type of PTC-component this is a reasonable approximation since, firstly, no explicit space-dependence is assumed for the material properties used in Eqs. (3.1) and (3.6), and secondly, the electro-thermal boundary conditions can be considered one dimensional so that the system is translationally symmetrical in two dimensions (this is explained in greater detail below). The reduction of the dimensionality of the model and its geometric interpretation is shown schematically in Fig. 9.

The system behaves effectively one dimensional with respect to the electrical boundary conditions, if it is assumed, that the plane electrode layers at $z = \pm h_{\mathrm{PTC}}/2$, which cover completely both flat surface areas of the disc, are electrical equipotential planes. The one-dimensionality holds also for the thermal boundary conditions for two reasons, namely (i) the solder covers completely both surface areas of the disc with a nearly constant thickness, so that the temperature is approximately equalised within the solder due to its good thermal conductivity, and (ii), the heat loss into the surrounding air through the surface shell of the disc is negligible compared to the heat flux into the solder-wire system so that this shell is considered as adiabatic. Nevertheless the heat loss (convection and radiation) through the lateral surface shell is taken into account by introducing an equivalent volume heat sink in the PTC-component.[20] Consequently the electrical current and the heat flux in a one dimensional approach is parallel to the component axis (z-axis) without any radial contributions. Additionally, by avoiding secondary geometric effects, the importance of taking the varistor-effect into account can be demonstrated much more clearly within the one dimensional model. Of course, the one-dimensional model will fail, if for instance, the connecting wire is point-soldered, or the gaps between the electrode and the ceramic rim are too large (as shown, e.g. in Fig. 9, left), or if the component is operated in a strongly cooling environment. As indicated in Fig. 9, a plane of symmetry allows a reduction to a half model without loss of generality. For this system, the following electro-thermal boundary conditions hold: the plane of symmetry (i.e. $z = 0$) is thermally adiabatic

$$\frac{\partial T(t,z)}{\partial z}|_{z=0} = 0. \tag{3.7}$$

and electrically fixed to zero potential. The end of the wire connected to the specimen holder is kept at ambient temperature at 24°C. The potential at the top of the disc (at $z = +h_{\mathrm{PTC}}/2$) has to be calculated for every point in time. This has to be done by an expression of the form:

$$\Phi(t,z)|_{z=h_{\mathrm{PTZC}}/2} = \frac{1}{2}(W(t) - V(t)) = \frac{1}{2}W(t)\cdot\left(1 - \frac{R_V}{R_V + R_{\mathrm{PTC}}(t)}\right). \tag{3.8}$$

Finally the required material properties of the solder and copper-wire, which are assumed to be temperature-independent, are summarised in Table 4. But since the diameters of the ceramic disc and the wire (and in general also the solder) is not identical, the tabulated values have to be adapted (these modified materials are called "quasi-wire" and "quasi-solder" in Fig. 9) to obtain the correct net heat fluxes.

After calculating the temperature field as a function of time and the axial coordinate of the disc, a standard thermo-elastic FEM-analysis is performed, which gives

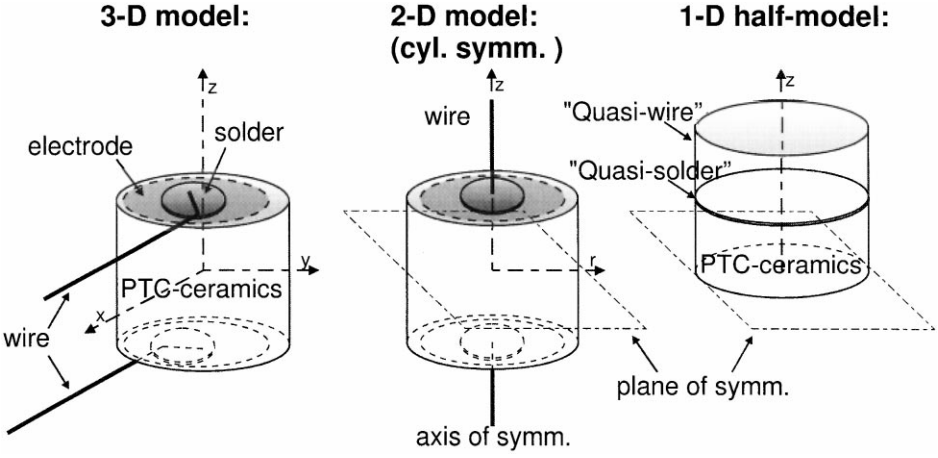

Fig. 9. Reduction of the dimensionality of a general model for PTC-components.

Table 4
List of material properties for solder and copper, as required for the electro-thermal analysis

Property	Units	Solder	Cu-wire
Mass density	kg/m^3	11400	8890
Specific heat capacity	J/kgK	129	385
Thermal conductivity	W/mK	35	386

a time-dependent strain- and stress-field within the ceramic disc corresponding to the thermal loading. The surfaces of the discs are considered as mechanically unclamped so that only internal thermal stresses occur in the initially at room temperature stress-free assumed sample. Since the Young's modulus and the yield stress of the solder is relatively small, the resulting influence of the thin solder layer is expected to be negligible. (If this mechanical interaction ceramic-solder should be included, also — to be accurate in the description — the residual stresses between the ceramic and the solder caused by the cooling process after the soldering procedure have to be taken into account, which are not known exactly at the one hand and expected to be small due to the low yield stress of the solder on the other hand.) For the sake of clarity and simplicity these minor effects are completely neglected.

3.1. Calculation of the probability of failure

PTC-ceramics under tensile load tend to fail by brittle cracking, which is a typical mode of failure for ceramics. This behaviour is a consequence of the fact that the yield strength is generally higher than the fracture strength of ceramic materials. In contrast to ductile materials (e.g. metals) the fracture criteria is fulfilled before peak stresses can be relaxed by plastic deformation, so when a tensile stress exceeds a certain critical threshold mechanical damage occurs by catastrophic crack propagation. Fracture initiation occurs at regions of high stress intensity around intrinsic material defects, e.g. pores and microcracks. Since the critical defects are distributed randomly in a component, the strength of a component is also a stochastical variable and can only be described in terms of probability. A well-established method to calculate probabilities of failure for tensile loaded ceramic parts is the Weibull approach.[21–23] A more detailed description of the probabilistic model can be found in the Ref. 24. Three material parameters characterise the probabilistic strength, namely the characteristic strength σ_0, a parameter m for describing the scatter of the strength, and a sample volume V_0. For the PTC-material under consideration these parameters were determined to 120 MPa, 15 and 0.3 mm^3 respectively and were found to be temperature-independent within the experimental error.[26] Since, however, the stress field $\sigma(t, \vec{x})$ within a PTC-component is time dependent, the Weibull theory has to be extended to include time-dependent stress-behaviour to calculate time-dependent probabilities of failure $P_f(t)$ [28]. The resulting generalised cumulative probability function can be written as:

$$P_f(t) = 1 - \exp\left[-\frac{1}{V_0} \int_{V_{PTC}} \left(\frac{\underset{0 \leqslant t' \leqslant t}{\mathrm{Max}} \left[\hat{\sigma}(t', \vec{x}) \right]}{\sigma_0} \right)^m \mathrm{d}V \right] \tag{3.9}$$

The scalar equivalent stress value $\hat{\sigma}$ for the numerator of the Weibull-integral in Eq. (3.9) is defined as the local maximum of the time envelope of the first principal stress between the starting time 0 and t. Consequently, the highest and "most dangerous" stress that appears at each location in the sample during the considered time span is taken into account. To obtain the rate of failure with respect to any time (designated in this paper as differential probability of failure), the monotonically increasing function (3.9) has to be derivated with respect to time.

In fact, there are also other possible mechanisms of mechanical failure, e.g. slow crack-growth (i.e. crack propagation in regions of undercritical load). In this work these have been neglected, since their effects are expected to be small in single switching tests conducted. For the interpretation of long-cycle tests, however, it would be necessary to generalise Eq. (3.9) to take the effect of slow crack-growth into account.[25,27]

4. Discussion of theoretical and experimental results

To demonstrate the main features of the electro-thermal behaviour of PTC-components, the results of DC-voltage driven switching processes are discussed in the following chapter. In this constant load case all observed variations in the current-signal with respect to time are caused only by changes in the resistance of the PTC-component. In addition, to investigate the varistor-effect more directly, the results of AC-tests, in which this effect is intrinsically more accentuated than in DC tests, are presented. Finally the fracture behaviour at high applied voltages, where mechanical damage to the PTC-samples occur, is discussed and fracture surfaces are interpreted.

4.1. DC-experiments

To perform a first test of the (parameter-free) mathematical model, three different voltages, namely 100, 200 and 300 V, were applied to a PTC-component connected in series to a shunt resistor of 1 kΩ. As described in Section 2.2 the total applied voltage and the resulting current were measured. To compare these data with the theoretical predictions for the same loading conditions,

corresponding (integral) values have to be derived from the respective field-quantities calculated with the mathematical model [Eqs. (3.1) and (3.6)].

The PTC-component is assumed to be homogeneous in all its material properties (i.e. without any explicit space-dependence), consequently the resistance field is also constant in the PTC-ceramic at any constant temperature. The measured total resistance of the PTC-resistor is plotted with respect to time as hollow symbols in Fig. 10. The resistances at the beginning of the tests are close to 128 Ω, which corresponds well with the zero load value of the resistance/temperature characteristics at ambient temperature, i.e. 24°C. The reduction in resistance due to the varistor-effect is relatively small since the electric field strength is low and nearly constant in the PTC-component at the beginning. The major voltage drop occurs in the shunt resistor. A mean field strength $\bar{E}$ can be calculated by solving the following implicit equation, where the electrical field is given as the quotient of the voltage drop at the PTC-component $U = W - V$ and the sample thickness h_{PTC}:

$$\bar{E} = \frac{U}{h_{\mathrm{PTC}}} = W \cdot \frac{R_V}{R_V + R_{\mathrm{PTC}}(T, \bar{E})} \cdot \frac{1}{h_{\mathrm{PTC}}}, \tag{4.1}$$

which at the start of the loading process yields initial values for electrical field strength of 45, 91 and 136 V/cm with respect to the three voltages (viz. 100, 200, 300 V) defined above. In the course of the self-heating process the total PTC-resistance first passes through a minimum value R_{min}, which is marked with arrows at different times in each load case in Fig. 10. Then the strong PTC-resistance increase occurs, and finally the resistance tends asymptotically to a voltage dependent stationary value, which is virtually reached about 1 min after the start for the considered experimental configuration. The timespan until the onset of the PTC-slope around the reference temperature is reached, depends on the heating rate, which is essentially given by the electric power P released in the PTC-component (the heat loss through the sample surfaces is negligible for this estimation):

$$P = J \cdot U = \frac{U^2}{R_{\mathrm{PTC}}} = J^2 \cdot R_{\mathrm{PTC}}. \tag{4.2}$$

The measured electric power is plotted in Fig. 11 for the same three experiments as shown in Fig. 10. The actual power maximum P_{max}, given by

$$P_{\mathrm{max}} = \frac{W^2}{4R_V}, \tag{4.3}$$

occurs when the PTC-resistance reaches the value of the shunt-resistor, namely 1 kΩ. These peaked maxima are marked by arrows (see. Fig. 11). After this power maximum is reached, a drastic fall of the electric power takes place and, in accordance to the asymptotic "long time" behaviour of PTC-resistance, a power limit is reached where heat generation and loss balance. The small inset in Fig. 11 (top, right) shows the inrush current with respect to time on a smaller timescale for the load cases, where 300 and 200 V were applied. Since the total resistance of the electrical circuit is initially dominated by the non-varying shunt-resistance, the total initial current is also nearly constant. Subsequently, the current decreases dramatically in concurrence with the resistance increase (see Fig. 10) of the PTC-component. These three experiments were simulated with the described model for the following two cases: (i) including the varistor-effect, and (ii), for direct comparison, also without varistor-effect. The results of simulation are plotted in Figs. 10 and 11 as solid lines and dashed lines respectively. Due to the small influence of the varistor-effect on the PTC-resistance in the low-temperature regime at the beginning, as mentioned above, the differences in the results of the simulations with and without taking the varistor-effect

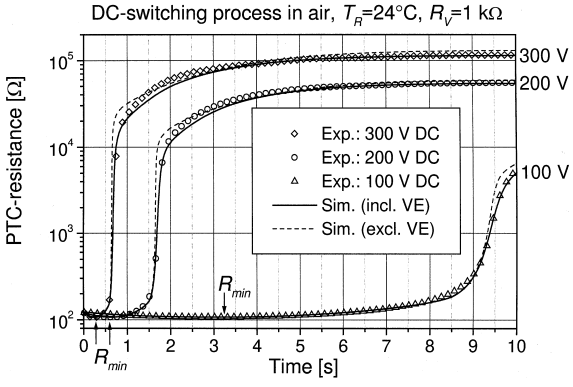

Fig. 10. Measured (symbols) and calculated total PTC-resistance with respect to time for 3 load cases (solid line: full model; dashed line: without varistor-effect). Inset: Inrush current on a larger time scale for 2 load cases.

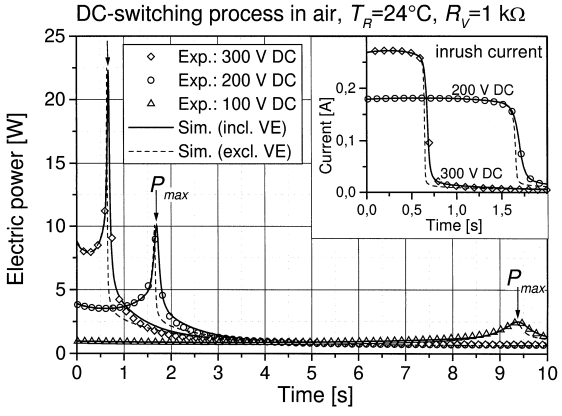

Fig. 11. Measured and calculated total electric power of the PTC-component with respect to time for 3 load cases (solid line: full model; dashed line: without varistor-effect). Inset: inrush current on a larger time scale for 2 load cases.

into account are initially negligible. But later, a stronger increase in the PTC-resistance and finally a higher value for the stationary PTC-resistance, compared to the experiment, is found in the simulation where the varistor-effect is neglected (dashed lines in figs. 10 and 11). A satisfactory agreement is found between the experimental data and the theoretical results where the varistor-effect was taken into account. The minor differences between the experimental data and the full simulation are caused by the restrictions of the one-dimensional model on the one hand (i.e. the small gap between the electrode layer and the rim of the disc and the non-constant thickness of the solder are neglected in the model), and the numerical (and basically arbitrary) extrapolation of the varistor-effect to high electric fields, according to the function defined in Appendix A, on the other hand. As will be shown in the following section, the electrical field strength is strongly inhomogeneous over the length of the axis of the PTC-disc and exceeds several times the field strengths used in the experimental determination of the varistor-effect. While integral variables, such as the total PTC-resistance and the total current, were measured, no measurements were performed to determine the space-dependence of the local temperature $T(t, z)$, resistance $\rho(t, z)$, electric field strength $E(t, z)$ and the electrical energy release rate $p(t, z)$. These quantities were only obtained by simulation. But the integral and the field-quantities are mapped on each other in the following way:

$$R_{\mathrm{PTC}}(t) = \frac{1}{r_{\mathrm{PTC}}^2 \cdot \pi} \int_0^{h_{\mathrm{PTC}}} \rho(t, z) \cdot \mathrm{d}z, \tag{4.4}$$

$$U(t) = \int_0^{h_{\mathrm{PTC}}} E(t, z) \cdot \mathrm{d}z, \tag{4.5}$$

$$P(t) = r_{\mathrm{PTC}}^2 \bullet \pi \bullet \int_0^{h_{\mathrm{PTC}}} p(t, z) \bullet \mathrm{d}z. \tag{4.6}$$

Since qualitatively similiar behavior was obtained for all load cases, only the results of the simulated load case with 300 V DC are presented in detail below. To show the influence of the varistor-effect on these space-dependent quantities, the results of simulations with and without the varistor-effect are compared.

Due to the inherently couplings of electrical and thermal processes, the corresponding quantities will be discussed together. In Figs. 12–15 sequences in time of the axial temperature, resistance, electric field and heat generation profiles are plotted for two half-models corresponding to the results with (right-hand side of each figure) and without (left-hand side of each figure) the varistor-effect. At the beginning the temperature is constant at 24°C (room temperature), which leads to a constant resistance, electric field strength and heat generation

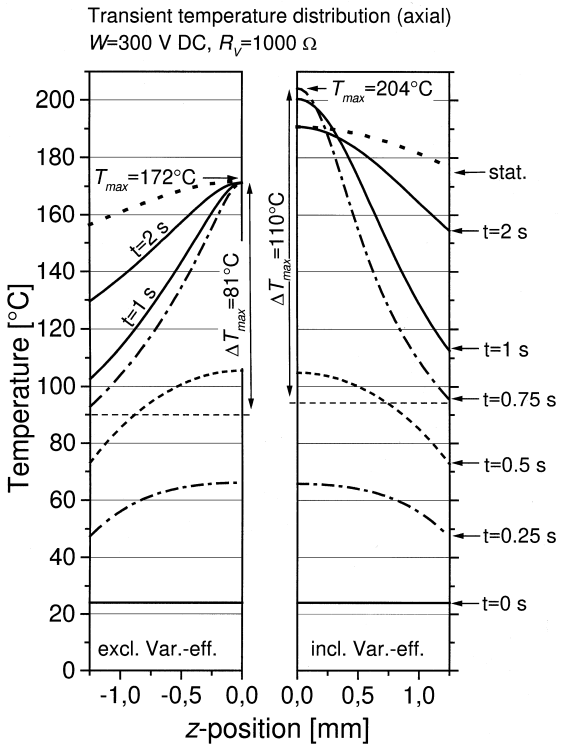

Fig. 12. Transient temperature profiles for the case with (r.h.s.) and without (l.h.s.) varistoreffect.

distribution. Although the heating rate, shown in Fig. 15, is nearly constant during the first 0.5 s, which is proportional to the resistance profile according Eq. (3.2), the temperature increase is significantly reduced near the disc's faces (at $z = \pm 1.25$ mm in Fig. 12) due to the cooling effect of the not actively heated solder. The central regions of the PTC-disc reach the reference temperature faster, so that the resistance increase starts locally in this range. A higher resistance leads to a concentration of the heat generation and consequently a strong temperature increase in the centre of the PTC-disc. This positive feedback causes, in the case without the varistor-effect, a temperature difference of about 80°C between the centre and the faces of the disc, under these boundary conditions. The full model inclusive the varistor-effect predicts an even stronger positive feedback-effect: a transient temperature-overshoot occurs in the centre and leads temporarily to a temperature maximum of more than 200°C; resulting in temperature differences of about 110°C. This specific feature is caused by the varistor-effect. When the more strongly heated centre changes to the high-resistance state, the voltage drop is also concentrated in the central region, as shown in Fig. 14. But high electric fields lead to a reduction of the resistance according the varistor-effect, so that a further heating process occurs until the temperature and the resistance are large enough to balance the electric power and the heat loss. The varistor-effect affects also the

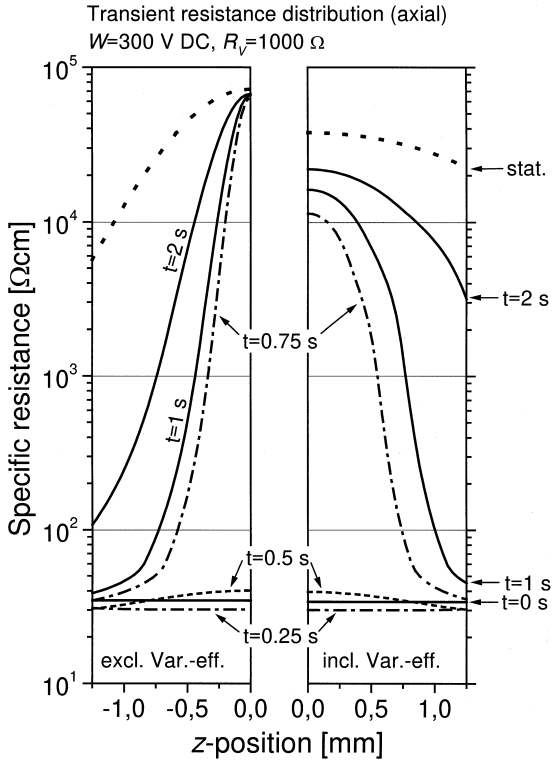

Fig. 13. Resistance profiles $\rho\,(t, z)$ for several timesteps, calculated for the case with (r.h.s.) and without (l.h.s.) varistor-effect.

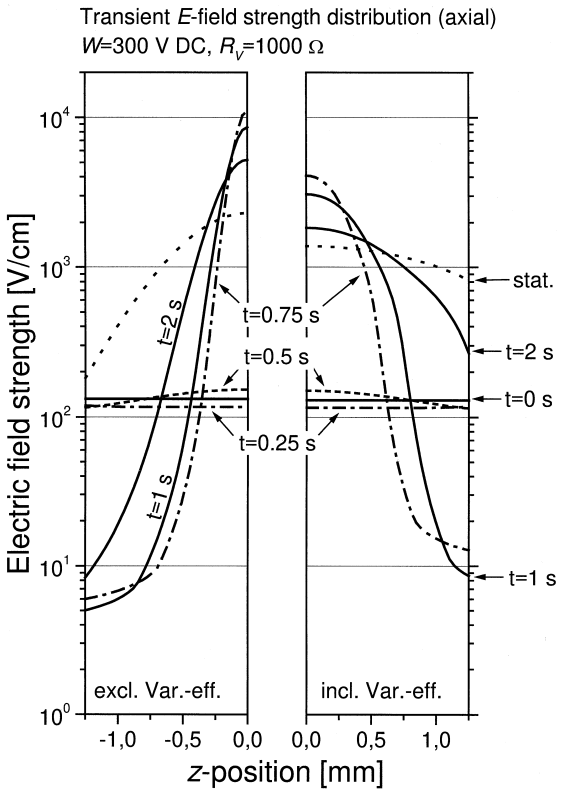

Fig. 14. Electric field strength profiles $E(t,z)$ for several timesteps, calculated for the case with (r.h.s.) and without (l.h.s.) varistor-effect.

maximum of the electric field strength, which is strongly reduced compared to the case without varistor-effect (Fig. 14), in which the highest calculated values of about 10 kV/cm would exceed the breakdown field strength. With time, the range of high resistance becomes broader due to internal heat conduction, and the corresponding reduction of the electric field goes hand in hand with an increase of the local resistance so that the temperature overshoot in the centre decays. Finally, the temperature converges to a stationary temperature profile, which differs by about 20°C between the centre and the top surface of the disc. The stationary temperature on the surface of the disc around the central symmetry-plane was determined by pyrometry to be about 190°C. This is in agreement with the results of the full simulation and is definitely above the prediction of the model without varistor-effect (i.e. 172°C). Thus the measured stationary values for the temperature and total resistance confirm that the assumptions in the full model are reasonable, and also prove the importance of taking the varistor-effect into account.

4.1.1. Calculation of the stress field

The previously described heating process causes a thermal expansion of the PTC-ceramic according to the temperature-dependent expansivity as shown in Fig. 5. Since the geometry of the axially varying temperature field is mirror symmetric with respect to the central

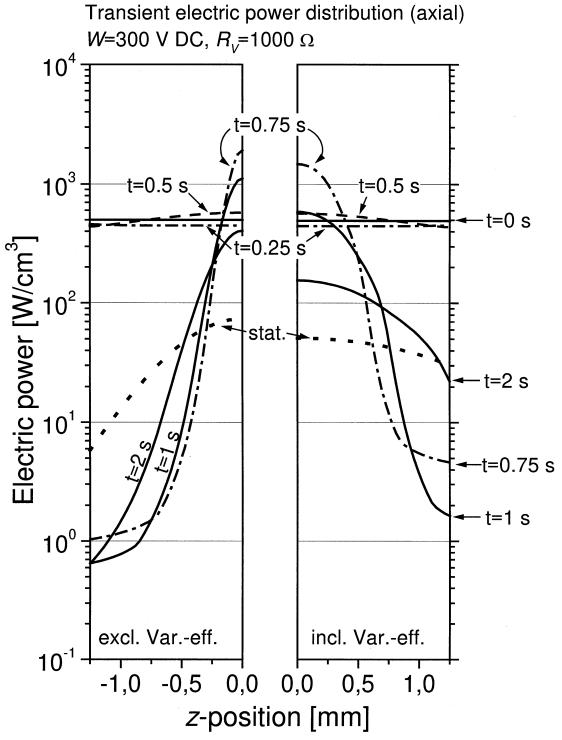

Fig. 15. Heat generation (electric power) profiles $\rho\,(t, z)$ for several timesteps, calculated for the case with (r.h.s.) and without (l.h.s.) varistor-effect.

plane, the expansion is internally constrained and thermal stresses occur.

Because all applied load cases lead to qualitatively similiar results, only the thermo-elastic results for the applied load of 300 V DC will be discussed in detail below. Where, however, significant differences to other load cases do occur, these will be mentioned. In Fig. 16 isobars on a cross-sectional area of the first principal stress field at that time of the greatest temperature difference are shown for the simulation including the varistor-effect. This stress field corresponds to the temperature profile at $t = 0.75$ s, shown as a dashed-dotted line on the r.h.s. of Fig. 12. While the centre of the ceramic disc is under a compressive stress, the outer regions are in tension. In the considered case a significant stress maximum of about 100 MPa occurs near the peripheral surface in the plane of symmetry between the electrode layers. This significant stress concentration is caused by the constraining effect of the relatively cold disc-faces, which clamp the thermal expansion of the warmer central planar regions. In Fig. 17 the evolution with respect to time of the stresses during the PTC-switching process is shown for two special points of symmetry. The solid line correspond to the stress evolution in the previously mentioned point on the plane of symmetry where the stress maximum occurs (designated "Pos. 1"). Corresponding to the development of the temperature field, a strong increase of the axial stresses occurs when the positive feedback driven temperature differences become larger. After passing the maximum in stress and temperature difference, the stress amplitudes decrease to moderate values. The dashed line shows the relatively low amplitude of radial stresses in the centre of the disc-face (designated "Pos. 2") with respect to time. For comparison, the dashed-dot line in Fig. 17 shows the stress evolution at Pos. 1 for the case without varistor-effect — although the maximum temperature difference is 81°C, which corresponds to about

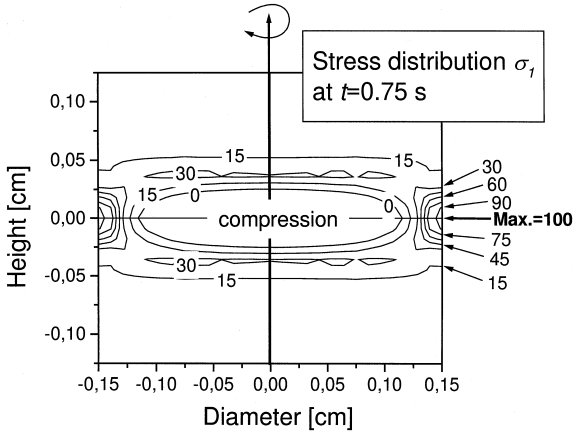

Fig. 16. Contour-line plot (isobars) on a cross-sectional area of the 1st principal stresses (in MPa) at $t \sim 0.75$ s, when the temperature differences are up to a maximum.

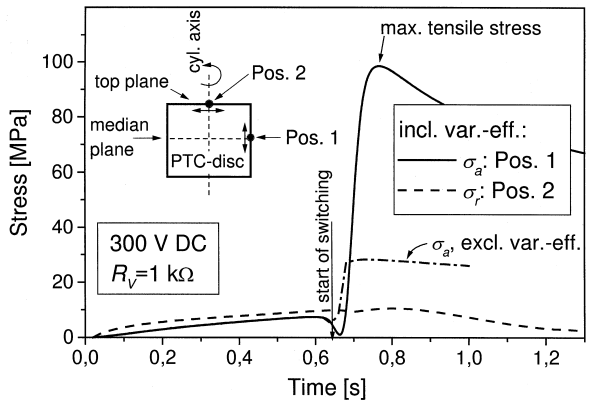

Fig. 17. Amplitude of stress with respect to time at two points of interest on the disc's surface.

75% of the value derived from the full simulation (incl. varistor-effect), the resulting maximum stress value is only 30%, i.e. 30 MPa. Indeed, stresses of this order of magnitude are also found in literature for PTC-models where the varistor-effect is not taken into account.[11] For materials with constant thermal expansion coefficient and Young's modulus, the stresses scale with the temperature difference. In the case of PTC-ceramics, of which the thermo-elastic properties are highly temperature dependent, both the temperature difference and the general temperature level have an effect on the amplitude of the thermo-mechanical stresses. In the simulated case, where the varistor-effect was included, the obtained temperatures were significantly higher so that a larger proportion of the ceramic was in the high temperature phase where the thermal expansion coefficient and the Young's modulus is much larger than at room temperature. This leads to the superproportional increase in the stress amplitude in the full model.

Experimental evidence corroborating the theoretically simulated stress amplitudes has been obtaind by conducting destructive switching tests at applied voltages where the calculated stress amplitudes actually exceed the measured material strength. These results will be discussed in Section 4.3.

4.2. AC-experiments

Applying an AC-voltage source to the PTC-circuit instead of a DC-source leads to modulated electric signals. A typical measured current signal for a case where the electrical root-mean-sqare (RMS) voltage was chosen to be 350 V is shown in Fig. 18a as a solid line; all other experimental conditions were kept as described in Section 4.1 above. The amplitude of the current-signal is large at the beginning, and decreases according to the PTC-effect. Since the source-voltage runs through the whole voltage range from zero to a maximum of ±495 V within every half sinoidal period (i.e. every 0.01 s), the corresponding resistance/electric field characteristics (varistor-effect) of

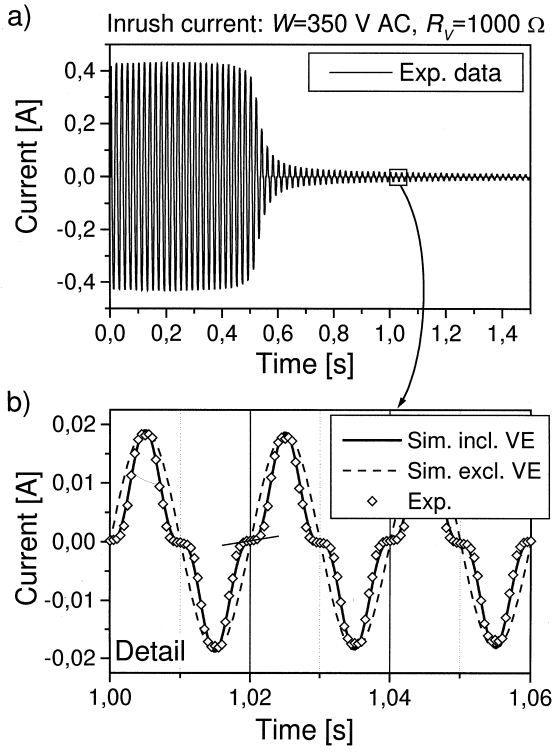

Fig. 18. Current signal during an AC-experiment at 350 V (a). The detailed plot (b) shows the deviations from a sinusoidal signal due to the varistor-effect in the time range from 1 to 1.06 s. The line at $t = 1.02$ s marks the slope at the AC-crossover.

the PTC-ceramics is scanned periodically. The detailed plot in Fig. 18b shows the actual measured (symbols) and calculated (solid line) current signal for three AC-periods for the timespan between 1 and 1.06 s. By this time the PTC-ceramics has changed to the high-temperature state, so that the majority of the applied voltage is consumed by the PTC-component. Significant deviations are found from a sinusoidal oscillation (dashed line), which would be the resulting signal of a hypothetic PTC-component without any varistor-effect (i.e. linear current/voltage characteristics at constant temperature). While the total PTC-resistance reaches the value of the zero load resistance during the AC-crossover at time $t_{\text{crossover}}$ (this value is essentially given by

$$R_{\text{PTC}}(t_{\text{crossover}}) = \frac{\partial J/\partial t}{\partial W/\partial t}|_{t_{\text{crossover}}} - R_V, \tag{4.7}$$

the ratio of the slopes of the current to the applied voltage — see tangent in Fig. 16b), the resistance is reduced more than an order of magnitude at the voltage peaks.

A comparison between the stress amplitudes simulated under DC and AC loads by using identical nominal voltages (for example 300 V AC, which is actually ±424 V peak-to-peak, and 300 V DC) shows that the stresses in the AC-driven PTC-component are about 5–10% higher. This stress amplification is again a consequence of the varistor-effect, which leads to superproportional electrical power release rates during the AC-voltage peaks. The larger net heating rate (i.e. the mean value of the modulated signal over one AC-period) leads to a sligthly higher temperature-overshoot, compared to the nominally equivalent DC-case, resulting, consequently, in higher thermo-mechanical stresses in the ceramics.

4.3. Interpretation of destructive electrical tests

To study the behaviour of fracture during the PTC-switching process, a set of several tens of samples was tested under electrical loads between 450 and 500 V AC. As before, a 1 kΩ shunt-resistor was used. Under these conditions 20–50% of the sample set failed due to partial cracking or complete delamination. The results of the mathematical model indicate two significant features, which are empirically verifiable, with regard to the timing and location of fracture.

1. A sudden stress maximum was found to form immediately after the strong PTC-resistance increase (compare Fig. 17). Therefore, it is expected that samples most probably fail within the time required from PTC-switching to reach the peak stress. In Fig. 19a, the observed times to failure, which are considered to occur when a concurrent discontinuity in the corresponding current signal is observed, are presented as a histogram. Additionally, the calculated differential probabitity of failure with respect to time is plotted as a solid line. The maximum of the probability density of failure occurs during the strong increase of the stress amplitude in time (Fig. 19b), which, on account of the higher applied voltage, occurs at earlier times than in the previously described examples. This is in agreement with the experiment. Further, this mode of failure was never observed in the initial time span where the total electric current is large which is also in conformity to the theory. (Note, within this time range, PTC-components are, however, susceptible to failure by the burning away of the electrodes.) Minor deviations between theory and experiment are found on the decreasing slope of the theoretical stress amplitude curve. Since the density of failure-probability is very sensitive to details of the stress distribution, the deviations may be caused either by deficiencies of the one-dimensional model or by slow crack growth.
2. The well defined stress maximum is found to be concentrated at the peripheral surface in the plane of symmetry between the electrodes. When a PTC-component fails due to a delamination fracture, the corresponding origin of fracture should be found in the fracture surface in the vincinity of this

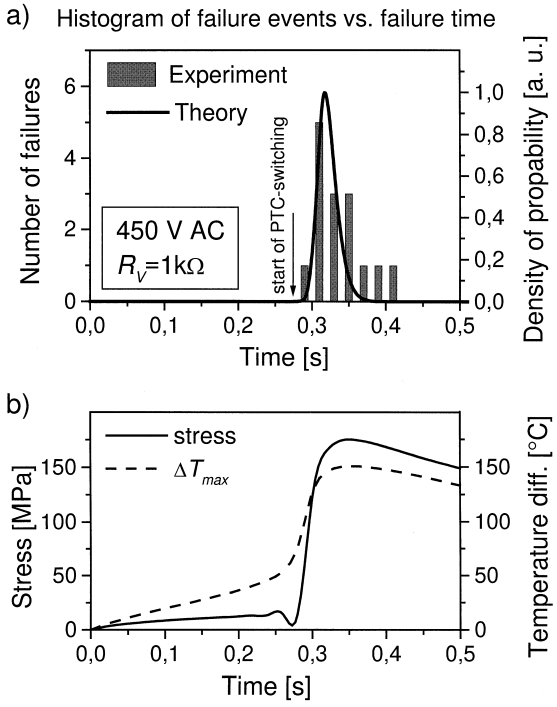

Fig. 19. (a) Histogram of times to failure compared to the calculated density of propability of failure for the load case of 450 V AC. (b) Corresponding maximum in stress and temperature difference with respect to time.

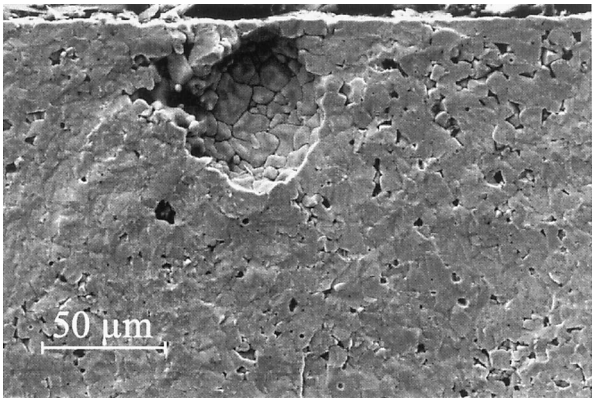

Fig. 20. A pore as fracture origin, directly under the surface.

ring-shaped region of stress maximum. By investigating fracture surfaces using scanning electron microscopy, it was possible to identify the defects which caused the fractures. In Figs. 20 and 21 two examples of fracture initiating defects, namely pores and badly sintered regions, are shown. They are found, as expected, on the plane of symmetry in the vincinity of the surface of the disc. Frequently, a step located diametrically opposite to the fracture origin, is found on the fracture surface. The step forms where the two crack fronts running around the disc meet together. Such a step is clearly evident at the bottom of the fracture

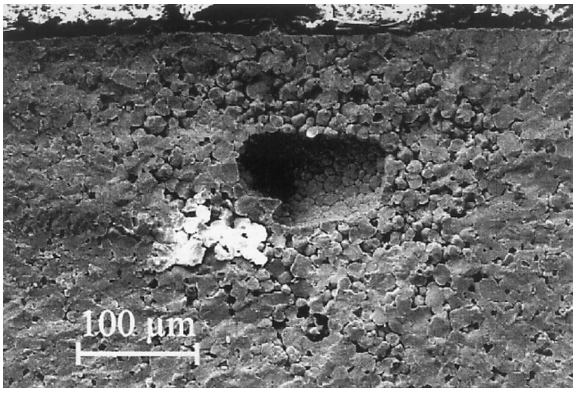

Fig. 21. A pore, surrounded by a badly sintered region, as fracture origin, close to the surface.

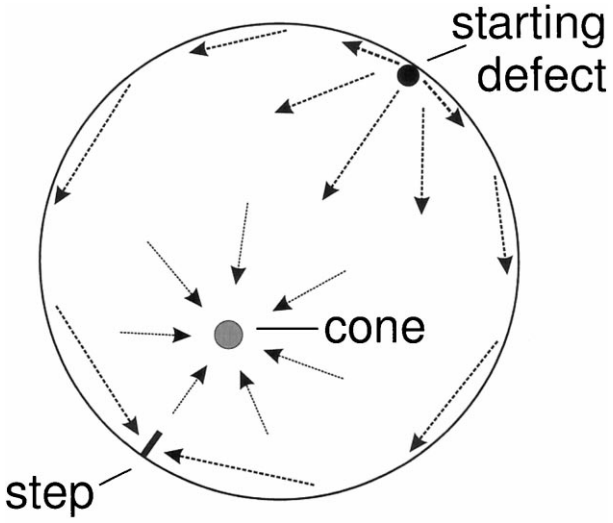

Fig. 22. Schematic representation of the mechanism of the delamination failure.

surfaces in Fig. 1. Finally, the crack runs to the centre of the disc and a more or less clearly cone-like structure (which was interpreted as the actual fracture origin by[7]) arises a little bit off-centre on the fracture surface. The mechanism of delamination fracture, which occurs at a speed approaching the velocity of sound, is shown schematically in Fig. 22.

5. Summary and conclusions

The electrical switching behaviour of soldered PTC-components was studied experimentally under different applied voltages. A one-dimensional mathematical model, including all relevant temperature-dependencies of the material properties, was developed to describe the electro-thermal thermistor processes. The varistor-effect (i.e. the electric field-dependeny) in the PTC-resistance/

temperature characteristics was specifically integrated into the model. Subsequently, a three-dimensional thermo-elastic analysis with a fracture-statistical interpretation of the calculated stress fields was performed. With respect to the electrical and thermal quantities, the results of the model are in a satisfactory agreement with AC and DC experiments. By performing destructive electrical tests at high applied voltages and analysing the fracture surfaces, the following predictions of the model were verified and confirmed.

1. The stress maximum was found at the periferal surface in the plane of symmetry between the electrode layers. The origins of fracture in delaminated PTC-samples, namely critical pores and defects, were actually detected within this ring-shaped area.
2. The failure-events were found to happen during a short time span in the order of one to several tenths of a second after the onset of the strong increase in PTC-resistance, which is in agreement to the calculated probability of failure with respect to time.

Whereas calculations including the varistor-effect appear to be realistic, those conducted without taking the varistor-effect into account yield transient and asymptotic temperatures, which are clearly too low to cause sufficient mechanical stress to exceed the material strength. Furthermore, high electric field strength of the magnitude predicted by excluding the varistor-effect would be high enough to cause electric breakdowns within the PTC-component.

In the present work, the varistor-effect has been measured in a narrow range of electric field strength due to limitations of the available equipment. Relevant data for the modelling has been attained by applying suitable (but arbitrary) extrapolations. Since, however, the varistor-effect is proven to have a strong influence on the operational behaviour and the thermo-elastic loading of the PTC-components, and to avoid the necessity of arbitrary extrapolation, further investigations are required to measure the PTC-resistance with respect to the electric field strengths in the full range they occur in switching processes (i.e. from zero load to several kV/cm).

To analyse nonsymmetrical PTC-components, the electro-thermal part of the model has to be extended to a full three-dimensional FEM-model which would allow the solution of the coupled system of electrical and thermal equations by using temperature-dependent material properties including the varistor-effect. For example, an extended model like this is necessary to simulate the behaviour of components which are point soldered, or clamped, to the contacting wire (i.e. under space-dependent thermal boundary conditions), or in which the gap of the electrode-layer at the rim of the disc is too large (i.e. under space-dependent electrical boundary conditions). A future work will deal with these problems.

Acknowledgements

The author would like to thank Siemens/Matsushita OHG. (Deutschlandsberg/Austria) for providing PTC-samples, and acknowledge the collaboration of I. Hahn (Research Labaratories, Siemens Munich), J. Riedler (Siemens/Matsushita, Deutschlandsberg/Austria) and T. Lube (ISFK/University of Leoben) for providing some of the requested material data and the helpful discussions on related topics to this work.

Appendix A: Mathematical treatment of the temperature- and field strength dependencies of the PTC-resistance

On the basis of experimental data, a continuous mathematical function will be derived to allow inter- and extrapolation of resistance values for any combination of temperature and electrical field strength in given ranges.

In a first step the accurate values for the zero-load curve $\rho_0(T)$ were fitted by a spline-function. The resulting curve was shown in Fig. 3 as the solid line. The trend of the resistance at higher field strengths and at fixed temperature is approximated by the first non-linear term of a Taylor series of a general (non-linear and symmetric) current-voltage relation.

This Taylor expansion can be used to describe the experimental data concerning the varistor-effect within the experimental error, which is larger for measurements applying high voltages. In this case a fit based on an higher order expansion may be instable. The resulting temperature- and field-dependent function $\rho(T, E)$ is written as:

$$\rho(T, E) = \rho_0(T) \cdot \frac{1}{1 + a_{\mathrm{var}}(T) \cdot E^2}, \tag{A.1}$$

where $a_{\mathrm{var}}(T)$ is a temperature-dependent positive coefficient, which is also a fitted by a spline function. This function (A.1) is related to a current J, by

$$J \propto \frac{E}{\rho_0(T)} \cdot \left(1 + a_{\mathrm{var}}(T) \cdot E^2\right). \tag{A.2}$$

A vanishing coefficient a_{var} leads to the well-known Ohmic law. For small electric field strength the function (A.1) converges to the zero load curve, while increasing the field strength leads to the observed reduction in resistance at any given temperature. In Fig. 3 the fitted resistance/temperature characteristics are shown as lines for four different electrical field strengths in the range from (nearly) zero to 1.5 kV/cm.

References

1. Heywang, W., Bariumtitanat als Sperrschichthalbleiter. *Solid State Electronics*, 1961, **3**, 51–58.
2. Heywang, W., Resistivity anomaly in doped barium titanate. *J. Am. Ceram. Soc.*, 1964, **47**, 484–490.
3. Jonker, G., Some aspects of semiconducting barium titanate. *Solid State Electronics*, 1964, **7**, 895–903.
4. Kulwicki, B. and Purdes, A., Diffusion potentials in $BaTiO_3$ and the theory of PTC materials. *Ferroelectrics*, 1970, **1**, 253–263.
5. Heywang, W., Semiconducting barium titanate. *J. Mat. Sci.*, 1971, **6**, 1214–1224.
6. Lubitz, K., Switching behaviour of power PTC resistors. *Ber. Dt. Keram. Ges.*, 1978, **55**(6), 322–324.
7. Kulwitzki, B. Instabilities in PTC resistors. In *Proceedings of the 6th International Symposium on the Applications of Ferroelectrics*. IEEE, Bethlehem, PA, 1986, pp. 656–664.
8. Ford, R. and Kahn, M. Positive temperature coefficient resistors as high power puls switches. In *Proceedings of the 6th International Symposium on the Applications of Ferroelectrics*. IEEE, Bethlehem, PA, 1986, pp. 669–772.
9. Mader, G., Meixner, H. and Kleinschmidt, P., Study of microscopic heat sources in semiconducting barium titanate ceramics. *J. Appl. Phys.*, 1984, **56**, 2832–2836.
10. Heinen, B. and Waser, R., Influence of the thickness and area of NiCr/Ag electrodes on the characteristics of $BaTiO_3$-ceramic based positive-temperature-coefficient thermistors. *J. Mat. Sci.*, 1998, **33**, 4603–4608.
11. Dewitte, C., Elst, R. and Delannay, F., On the mechanism of delamination fracture of $BaTiO_3$-based PTC thermistors. *J. Eur. Ceram. Soc.*, 1994, **14**, 481–492.
12. Smith, D. S., Ghayoub, N., Charissou, I., Bellon, O. and Abelard, P., Transient thermal gradients in barium titanate positive temperature coefficient (PTC) thermistors. *J. Am. Ceram. Soc.*, 1998, **81**, 1789–1796.
13. Mader, G., Meixner, H. and Kleinschmidt, P., Mechanism of electrical conductivity in semiconducting barium titanate ceramics. *Siemens Forsch.-u. Entwickl.-Ber.*, 1987, **16**(2), 76–82.
14. Supancic, P. Mechanische Stabilität von keramischen Kaltleiterbauteilen - experimentelle Untersuchung und Theoretische Modellierung, PhD thesis, University of Leoben, Austria, 1998.
15. Hahn, I., Rettig, U. Bast, U. Materialkennwerte und Thermoschockverhalten funktionskeramischer Werkstoffe, Internal report/Siemens, Munich, 1996.
16. Hahn, I., Rettig, U., Bast, U., Riedler, J. Thermomechanical behaviour of positive temperature coefficient resistors under pure thermal shock loading. In *Proc. of Electroceramics V,* Portugal, 2–4 September 1996, pp. 475–478.
17. G. Mader, H. Meixner, P. Kleinschmidt, Temperature and stress dependence of Young's modulus in semiconducting barium titanate ceramics, *J. Appl. Phys.* **58** (1985) 702–704.
18. Parkus, H., *Thermoelasticity*, 2nd ed. Springer Verlag, Wien, NewYork, 1976.
19. Incropera, F. and DeWitt, D., *Fundamentals of Heat and Mass transfer*, 4th ed. John Wiley and Sons, New York, 1996.
20. Carslaw, H. and Jaeger, J., *Conduction of Heat in Solids*, 2nd ed. Claredon Press, Oxford, 1959.
21. Weibull, W. A statistical theory of the strength of materials. *Proc. Ing. Vetenskapsakad. Akad.* 1939, **151**.
22. Weibull, W., A statistical distribution function of wide applicability. *J. Appl. Mech.*, 1939, **18**, 293–297.
23. Freudenthal, A., Statistical approach to brittle fracture. In *Fracture: An Advanced Treatise, Vol. II: Mathematical Fundamentals*, ed. H. Liebowitz. Academic Press, New York, 1968, pp. 591–619.
24. Danzer, R., A general strength distribution function for brittle materials. *J. Eur. Ceram. Soc.*, 1992, **10**, 461.
25. Fett, T. and Munz, D., *Mechanisches Verhalten keramischer Werkstoffe*. Springer-Verlag, Berlin, 1989.
26. Geith, M. Mechanische Eigenschaften von Elektrokeramik. Diploma thesis, University of Leoben, Austria, 1998.
27. Danzer, R., Subcritical crack growth in ceramics. In *The Encyclopedia of Advanced Materials*, ed. D. Blooretal. Elsevier Science, Oxford, 1994, pp. 2693–2698.
28. Danzer, R., Fischer, F. and Yan, W., A dynamic tension test for ceramics — application of probabilistic fracture mechanics to a dynamic loading situation. *J. Eur. Ceram. Soc.*, submitted.